Heliyon 10 (2024) e26050

Contents lists available at ScienceDirect

Heliyon

journal homepage: www.cell.com/heliyon

Research article

Enhancement of microstructural and magnetic properties of high spin Mn substituted nanocrystalline Ni–Mn–Cu–Zn ferrites

Abdul Ahad , A.K.M. Akther Hossain *

Department of Physics, Bangladesh University of Engineering & Technology, Dhaka, 1000, Bangladesh

ARTICLE INFO

Keywords:
Auto combustion
Nanomaterials
Grain growth
Saturation magnetization

ABSTRACT

Mn-substituted Cu and Zn co-doped spinel-typed nano-crystalline ferrites having nominal composition $Ni_{0.50-x}Mn_xCu_{0.15}Zn_{0.35}Fe_2O_4$ (x = 0.00–0.25 in 0.05 increments) have been prepared through the citric acid assisted sol-gel auto-combustion technique. From the XRD measurements, it was found that several intense peaks ensured the cubic spinel-based ferrite structure beyond the formation of any impurity peaks. The crystallite sizes varied from 20 to 28 nm for ash-burnt powders following the coalescence process that decreased the lattice defects and strain. With an increase in Mn concentration, the hopping length (L_A) of the tetrahedral A-site increases, while the hopping length (L_B) of the octahedral B-site decreases with enhanced lattice constant. The sintered samples' average grain sizes, as measured using the Field Emission Scanning Micrographs (FESEM), differed from around 1.40 to 5.30 μm. Incorporating Mn-ion accelerates grain growth and crystallite size with increased bulk density and reduced porosity due to heat treatment. For increasing sintering temperature along with Mn concentration, porosity drops from 42% to 3%, resulting in enhancing the magnetic induction of the prepared ferrites. The 25% Mn substituted composition displays the maximum initial permeability ($\mu_i^{'} = 315$), which is ~7 times larger than the pristine composition. Due to the reduction of Ni content, the relative quality factor rises but the magnetic loss tangent reduces. An increased trends of $\mu_i^{'}$ are accompanied by decreased resonant frequency, obeying Snoek's law. According to the experimental findings, the high spin Mn substitution in the composition causes the saturation magnetization to increase while the coercivity and Néel temperature drop with increasing grain size. Hence, the locally prepared low-cost Nano-crystalline Ni–Mn–Cu–Zn ferrites bearing excellent properties can be a good candidate for promising future applications in nanotechnology.

1. Introduction

Now, it's the age of nanotechnology; people are trying to store a lot of information in a tiny space. Ferrite materials contain high storage memory with a small format size. Nano-sized ferrites are being exploited to meet these demands. Applications for ferrites include energy storage, data storage, electronics, magnetic sensing, chemical sensors, transducers, transformers, actuators, electrical devices, healthcare, and magnetic tape technology [1]. Ferrites are ferrimagnetic materials with one or more other metallic elements such as zinc, nickel, barium, and manganese. Ferrites are classified as hard ferrites and soft ferrites. Further, depending on the crystalline structure of ferrites they can also be categorized as ortho ferrites, spinel ferrites, hexagonal ferrites, and garnets. Spinel-type

* Corresponding author.
E-mail address: akmhossain@phy.buet.ac.bd (A.K.M.A. Hossain).

https://doi.org/10.1016/j.heliyon.2024.e26050
Received 1 December 2023; Received in revised form 7 February 2024; Accepted 7 February 2024
Available online 15 February 2024

ferrites have a chemical formula of AB_2O_4, with A being tetrahedral and B being the octahedral coordinated cations. Spinel-type ferrites with uniform particle sizes are used in targeted drug delivery, magnetic hyperthermia, medical imaging, and water purification due to their unique characteristics [2,3]. Garnet is one type of ferrite containing the chemical formula B_3 (Fe_5O_{12}), where B is yttrium or rare-earth ions. Ortho ferrite consists of an orthorhombic crystal structure with the formula $LFeO_3$, where L is one or more rare-earth elements. Hexagonal ferrites have a hexagonal crystal structure and high anisotropy along the c axis, whose familiar member is $BaFe_{12}O_{19}$, also called barium ferrite or M-type hexaferrites a type of barium ferrite, has a similar crystalline structure to magneto-plumbite, $PbFe_{12}O_{19}$, first studied by Adelskold in 1938. Barium hexagonal ($BaFe_{12}O_{19}$) BFO ferrite and reliable solutions based on it have gained interest because of their excellent characteristics. The space group p_63/mmc is a member of the hexagonal structure. Magnetic field-induced electric polarizations are also investigated in the doped [4,5] M-type hexaferrites. It was reported as to these hexaferrites that tailoring the characteristic in the ~20–65 GHz frequency range is of great practical interest. Hexaferrites [6] are widely used as permanent magnets, with over 80% of commercial permanent magnets being hexagonal ferrites. Recent publications on hexagonal ferrites have also expanded due to the new outcome of multiferroic characteristics materials that are active at room temperature showing the ferroic properties.

Top-down and bottom-up are the two principal methods to synthesize nanoparticles-in the top-down method, the bulk material is converted into powder and then nanoparticles, while in the bottom-up method, atoms are first formed into clusters and then into nanoparticles. Nano-sized materials are generally synthesized using physical, chemical, and biological methods. Ball milling [7], conventional ceramic (or solid-state reaction) [8], ion beam lithography (IBL), electron beam lithography (EBL), and spray pyrolysis techniques, etc., belong to the physical methods to synthesize nanomaterials. The chemical methods are co-precipitation [9], sonochemical, sol-gel, pyrolysis, phytochemical, solvothermal, and sol-gel auto combustion route, etc. Using plants and their extracts, microorganisms (bacteria, fungi, and actinomycetes), enzymes, biomolecules, agricultural and industrial wastage nanoparticles are synthesized biologically. Hence, using the different conventional and nonconventional routes powder forms of Nano-crystalline ferrites are formed in which ferrites' property is strongly dependent on the making procedure, as well as the ingredients of the nominal composition.

Due to exceptional functional characteristics, spinel-typed ferrites are the focus of ardent theoretical and experimental investigation for high-tech applications. The nano-crystalline mixed typed spinel ferrites are different at the nanoscale when they are comparable to their bulk complements. In many applications, nano-sized spinel-ferrites with uniform particle size are preferred.

Bueno et al. [10] reported about the manganese-doped Ni–Zn ferrite using the citrate-nitrate precursor route. Bhise et al. [11] also reported the effect of Mn incorporation in Zn–Ni ferrites through conventional ceramic techniques. The outcome of Mn ions substitution on functional characteristics features of $Ni_{0.6-t}Mn_tZn_{0.4}Fe_2O_4$ prepared via conventional solid-state reaction route has been investigated by Sattar et al. [12], and substitution results of manganese ion on the electromagnetic properties in $Ni_{0.5-x}Mn_xZn_{0.5}Fe_2O_4$ have been reviewed by Shirsath et al. [13].

Wani et al. [14] synthesized $Ni_xZn_{1-x}Fe_2O_4$ via glycine-assisted auto-combustion route in which they found that Zn spinel nano-ferrites exhibit paramagnetic behavior at 0% Ni content, and Ni–Zn spinel nano-ferrites show soft ferrimagnetic behavior at 25% Ni content. Besides, with increased Ni content, both saturation magnetization and coercivity are increased, suggesting their potential for photo-catalytic and high-frequency applications.

The study of magnetic behavior using a Vibrating Sample Magnetometer (VSM) revealed that samples transition from ferrimagnetic to ferromagnetic with substitution, potentially aiding in developing future sensing materials. The low-sensing response ferrites show potential for permanent magnet applications and high porosity, making them suitable for humidity sensor applications [15].

Batoo et al. [16] prepared Co–Zn ferrites nanoparticles through the auto-combustion route, and their experimental results concluded the shielding properties of materials' electromagnetic interference (EMI), which are generally initiated by the special effects of various losses, including magnetic core loss and dielectric loss, of prepared ferrites. Co–Zn ferrite is one of the most promising options for a shielding material. Additionally, it was noticed that Co–Zn nanoparticles' EMI shielding capabilities may be adjusted through appropriate doping or the fabrication of a composite material.

The Co–Cu–Zn nano-ferrite was prepared via the auto-combustion route [17] and it was noticed that with increasing Cu content, the crystallite size decreased. At the same time, high DC resistivity was recorded at 20% Cu concentration, indicating that the synthesized materials apply to high-frequency-based microwave electronic devices.

Hadi et al. [18] synthesized the ferrite nanoparticles in which dielectric spectroscopy indicated the Maxwell-Wagner interfacial polarization and minimal dielectric loss, enabling multilayer inductor chip fabrication.

Although there are other methods for preparing ferrite nanoparticles [1,7,9,10], the sol-gel auto combustion technique [15] is being extensively used because of its many advantages, including affordability, dependability, adaptability, and convenience of use. The extrinsic characteristics of Nickel Copper Zinc ferrites are improved through substituting specific transition metal ions, even though additives are frequently opposed to the electromagnetic properties of the synthesized ferrite materials. Ni–Mn–Zn, Ni–Zn, Li–Zn, and Ni–Cu–Co, etc., ferrites are synthesized and studied widely [19–21].

Still, the research on combining the spinel type Ni–Mn–Cu–Zn mixed ferrite prepared via sol-gel auto-combustion approach has not been investigated expansively. In addition, with uniform particle size distribution Ni–Cu–Mn–Zn ferrites materials have enhanced functional properties than that of Mg–Mn–Zn, Li–Zn, Ni–Co, etc. ferrites. If the functional properties can be effectively improved then the mixed spinel-type ferrites have potential applications for the fabrication of electronic devices We aim to find a relationship among the crystallite size, grain size, hopping length, Néel temperature, and coercivity and how they influence the electromagnetic, surface morphological and the structural properties of Mn substituted citric acid assisted Ni–Mn–Cu–Zn ferrites. Mn is a d-block paramagnetic element belonging to [Ar] $3d^54s^2$ electron configuration having a high spin magnetic moment ~5 μ_B. Hence, a minor Mn substitution instead of Ni bearing spin magnetic moment ~2 μ_B in the Ni–Mn–Cu–Zn ferrite system with promising x = 0.00–0.25 content may

change the functional properties. The Mn-substituted Ni–Mn–Cu–Zn spinel-typed nano-crystalline ferrites may govern the crystallite size, grain size, hopping length, transition temperature, and coercivity. Keeping these points in view, Cu and Zn co-doped $Ni_{0.5-x}Mn_xCu_{0.15}Zn_{0.35}Fe_2O_4$ (x = 0.00–0.25 in 0.05 increments) prepared through a sol-gel auto-combustion approach. The present research work investigated the structural, surface morphological, electrical, and magnetic properties of Mn-substituted Ni–Cu–Zn ferrites using the citric acid-assisted sol-gel auto-combustion approach. The synthesis of Ni–Mn–Cu–Zn ferrite nanoparticles using citric acid as a fuel and the produced nanoparticles (NPs) with their low coercivity and high permeability characteristics in medical applications like cancer treatment and high-frequency-based electronic devices make this work novel.

2. Experimental

2.1. Materials and method

The non-conventional sol-gel auto-combustion is a bottom-up approach [16] to synthesizing nano-sized spinel-type ferrites. The highly exothermic reaction between the fuel and nitrates is employed in the auto-combustion technique to synthesize nano-sized ferrites. As raw materials, the analytical grade of $[Ni(NO_3)_2{\cdot}6H_2O]$ (Nickel nitrate), $[Zn(NO_3)_2{\cdot}6H_2O]$ (Zinc nitrate), $[Cu(NO_3)_2{\cdot}3H_2O]$ (Copper nitrate), $[Fe(NO_3)_3{\cdot}9H_2O]$ (Iron nitrate), $Mncl_2.4H_2O$ (Manganese II tetra hydrate chloride), and $C_6H_6O_7$ (citric acid) was used in which 1 : 3 was the ratio of metal nitrate to citric acid, as well as 1 : 1 was also the molar ratio of metal nitrate to citric acid as shown in the flow chart (Fig. 1). And these used chemicals were analytical reagents marked with a purity of ≥99.9%. Citric acid as a fuel is used in the solution to accelerate the ignition rate. Using ammonia ($NH_3{\cdot}H_2O$) the pH ~7.0 value remained constant in the solution. The whole mixture of the composition was set up on the magnetic stirrer keeping a constant temperature at 150 °C; after several hours, the mixed solution was converted into sol and then into a gel form; after 6–7 h, auto combustion took place, and ash-burned powder of $Ni_{0.5-x}Mn_xCu_{0.15}Zn_{0.35}Fe_2O_4$ was processed. Nano-powders were used to make samples of pellet and toroid shapes by binding them with polyvinyl alcohol. With a heating ramp of 5 °C/min as well as a cooling ramp of 10 °C/min these investigated samples were heated at a temperature range of 900–1300 °C for 5 h.

2.2. Measurement and characterization

X-ray diffraction was carried out using an X-ray diffractometer that was equipped with monochromatic Cu-Kα radiation at a wavelength of 1.54178 Å. Using the XRD data, the crystallite size was estimated by the following Debye Scherer's equation [22]:

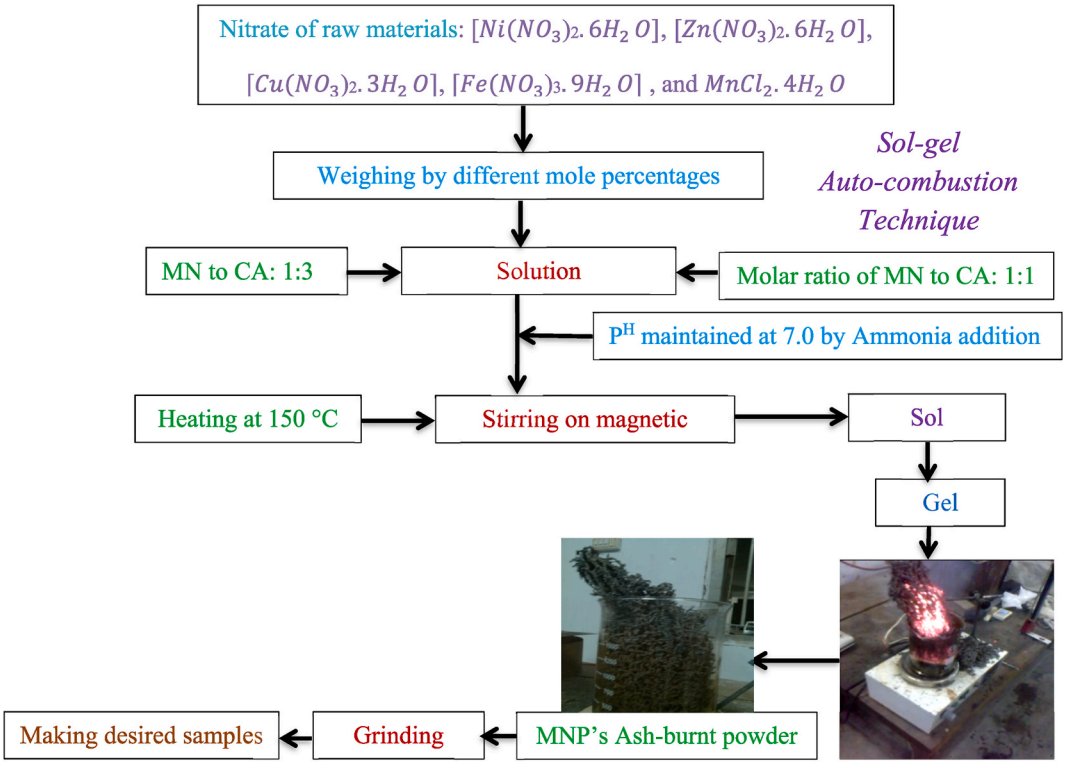

Fig. 1. Flow chart of stages in preparation of Nanocrystalline samples.

$$D_c = \frac{0.9\lambda}{\beta \cos\theta},$$

where D_c indicates the crystallite size, β defines the full width at half maximum, and λ is the wavelength of radiation.

Linear intercept method, which is used to measure the average grain diameter of the samples from the Field Emission Scanning Electron Micrographs (FESEM) [23].

The formula for calculating bulk density in a water medium was derived from the Archimedes principle: $\rho_{bulk} = \frac{W_a \rho}{W - W'}$,

where w_a represents the sample's weight in the air, W' symbolizes the sample's weight in water medium, and ρ defines water's density at room temperature.

The following equation was used to calculate the theoretical density ,ρ_{th}:

$$\rho_{th} = \frac{8M}{N_{Av} a^3} \; g \Big/ cm^3,$$

where N_{Av} is termed as Avogadro's number (6.023×10^{23}), M defines the molecular weight, and a is the lattice parameter.

Porosity, P % can be calculated using this equation: $P\% = \{100(\rho_{th} - \rho_{bulk})/\rho_{th}\}\%$, where ρ_{bulk} defines the bulk density measured by the principle of Archimedes.

A Wayne Kerr impedance analyzer (model no. 6520A) is used to determine the complex permeability keeping the frequency range 20–120 MHz, and the following equations are used to determine the real part of initial permeability, μ_i' and the imaginary part of initial permeability, μ_i'' [24]:

$$\mu_i' = \frac{L_s}{L_{coil}}, \mu_i'' = \mu_i' \tan\delta,$$

where L_s defines the self-inductance of the sample core.

and $L_{coil} = \frac{\mu_0 N^2 S}{\pi d_{mean}}$,

where L_{coil} indicates the inductance of the winding coil excluding the sample core, which is derived geometrically, where $N = 5$, gives the number of turns of the coil, and S also the cross-sectional area of the toroid samples as $S = d \times H$, here, $d_{mean} = \frac{d_2 - d_1}{2}$, d_1, and d_2 define the inner and the outer diameter respectively, $H =$ height, and $d_{mean} = \frac{d_1 + d_2}{2}$ being the mean diameter of the toroid samples and $\tan\delta$ the magnetic loss tangent of the prepared samples.

The relative quality factors (RQF) can also be determined by using this equation:

$Q = \frac{\mu_i'}{\tan\delta}$, where $\tan\delta$ defines the magnetic loss of the prepared materials.

From the temperature-dependent initial permeability, Néel temperature is also obtained. In this case, the prepared sample is placed in the oven with a thermocouple, and a fixed frequency (100 kHz) containing a sinusoidal wave is ensured in the impedance analyzer. Following this procedure by an impedance analyzer, the temperature-dependent permeability is calculated. As a function of the applied field (M − H), the saturation magnetization, M_s, and the coercivity, M_s both are measured by a VSM.

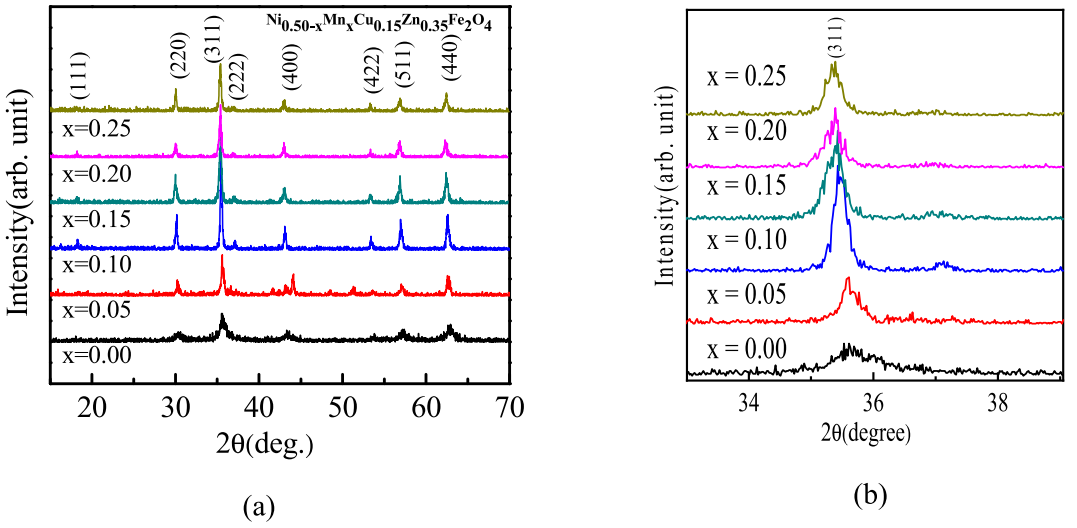

Fig. 2. (a) X-ray diffraction pattern of as-prepared powder, and **(b)** highest intensity peak of nanocrystalline $Ni_{0.50-x}Mn_xCu_{0.15}Zn_{0.35}Fe_2O_4$.

3. Results and discussion

3.1. Structural analysis and phase identification

The XRD patterns of the Mn substituted as as-prepared powders of $Ni_{0.50-x}Mn_xCu_{0.15}Zn_{0.35}Fe_2O_4$ with x = 0.00–0.25 are displayed in Fig. 2(a). From the XRD, it was found several intense peaks from (111), (220), (311), (222), (400), (422), (511), and (440) crystal planes. The position of the peaks confirmed the cubic spinel structure of these ferrites except for forming any impurity peaks, as proven by the JCPDS card No. 08–0234. With increasing Mn ion substitution in $Ni_{0.50-x}Mn_xCu_{0.15}Zn_{0.35}Fe_2O_4$ system the lattice constant, a_0 rises as shown in Fig. 3. The compositions follow Vegard's rule, which explains the relationship between the ionic radii and increased lattice constant with increasing Mn concentration. The lattice parameter, lattice constant, and unit cell belong to the ionic sizes of the substituted materials. In the prepared materials, the ionic radius of Mn ion is ≈ 0.89 Å, which is larger than the ionic radius of Ni ion ≈ 0.77 Å [1]. The ability of a unit cell to be squeezed or stretched depends on the ionic radii of the substituted materials.

The unit cell characteristic is also related to the prepared samples' oxygen deficiency. According to Tyunina et al. [25], introducing a slight oxygen deficiency can increase the lattice strain in the thin films of perovskite oxide. Anisotropic local stresses are produced around oxygen vacancies by lattice distortion, which interacts with the thin films' misfit strain. Thus, some crystallographic orientations of the stresses are energetically advantageous and can promote the epitaxial development of strained films.

However, for introducing larger manganese ions instead of smaller nickel ions into the lattice then the unit cell tends to be extended to conserve the complete cubic symmetry. Therefore, the average ionic radius ,$r_{variant}$ of the variation ions for $Ni_{0.5-x}Mn_xCu_{0.15}Zn_{0.35}Fe_2O_4$ system is termed as

$$r_{variant} = (0.50 - x)r_{Ni} + xr_{Mn}, \quad (1)$$

where r_{Ni} defines the ionic radius of Ni (≈ 0.77 Å), and r_{Mn} defines the ionic radius of Mn ion (≈ 0.89 Å). Equation (1) shows that ionic radii of Mn and Ni ions are key factors in changing $r_{variant}$. According to Fig. 3, the fluctuation $r_{variant}$ with increasing Mn concentration demonstrates that for the incorporation of large Mn ions instead of the small Ni ions the lattice constants increase showing an increased trend of $r_{variant}$.

3.2. Lattice constant, density, and porosity

XRD patterns of the as-prepared nano-sized powders of synthesized compositions are shown in Fig. 2(b), where (311) is the most significant intense peak moving from the right to the left side due to driving expansion for increasing lattice constant. It was observed that for substitution Mn content the value of β (full width at half maximum) decreases. Tables 1 and 2 provide data on the density (bulk and theoretical) and porosity of different $Ni_{0.50-x}Mn_xCu_{0.15}Zn_{0.35}Fe_2O_4$ samples. Fig. 4 shows that bulk density, ρ_{bulk} varied within the range of ~3.02–4.70 g/cm^3 when the samples sintered at 900–1300 °C, while theoretical density, ρ_{th} decreased from ~5.56 to 4.1 g/cm^3. The lessening in ρ_{th} can be ascribed to the rise in the lattice parameter and the resulting growth in crystallite volume. Besides these, the reduction in ρ_{th} can also be explained by different specific gravities of Mn, Ni, Cu, Zn, and Fe oxides. The ionic radius of Ni and Mn are 0.77 and 0.89 Å, respectively, suggesting that Mn has a greater ionic radius than Ni. As a result, the lattice parameter along with the unit cell tends to be increased when Mn substitution increases, which causes an immediate drop in the theoretical density. Fig. 5 demonstrated that with lessening Ni concentration ($0.00 \leq x \leq 0.25$) and increasing Mn concentration ($0 \leq x \leq 0.25$) in $Ni_{0.50-x}Mn_xCu_{0.15}Zn_{0.35}Fe_2O_4$ composition, ρ_{th} and porosity (P %) decrease but ρ_{bulk} increases. In contrast, with an increase in sintering temperature along with Mn concentration porosity drops from 42% to 3% resulting in promoting the density of the synthesized materials. An increase in bulk density in $Ni_{0.50-x}Mn_xCu_{0.15}Zn_{0.35}Fe_2O_4$ that fact can be overcome by the variation in the specific gravity of manganese, nickel, copper, and zinc oxides [26] and by the atomic weight of nickel and manganese [27]. The specific gravity of Mn,

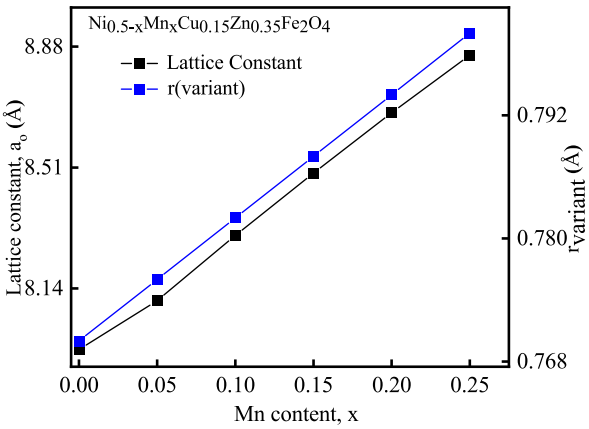

Fig. 3. Variation of lattice constant with Mn content, x, for as-prepared powder of $Ni_{0.50-x}Mn_x\ Cu_{0.15}Zn_{0.35}Fe_2O_4$.

Table 1
Lattice **constant**, crystallite size, x-ray density, average particle size, saturation magnetization, and coercivity of typical samples.

Mn content, X	*Lattice constant, a_0 (Å)*	*Crystallite size, D (nm)*	*X-ray density, ρ_{X-ray} (g/cm^3)*	*Average particle size of ash-burnt powder (nm)*	*Saturation magnetization, M_s (emu/g)*	*Coercivity, H_c KA/m*
0.00	8.0005	20	5.56	69	34.31	5.71
0.05	8.1024	24	5.50	90	37.40	5.68
0.10	8.3019	25	5.32	94	38.29	5.50
0.15	8.4929	26	5.33	96	45.12	5.40
0.20	8.6776	27	5.27	110	50.30	5.31
0.25	8.8544	28	4.12	126	54.95	5.20

Table 2
Sintering temperature, bulk density, porosity, resonance frequency, and permeability of the various $Ni_{0.50-x}Mn_xCu_{0.15}Zn_{0.35}Fe_2O_4$ sintered at various temperatures with a fixed dwell time of 5 h.

Mn Content	*Sintering Temp., T_s (^0C)*	*Bulk density, ρ_B (g/cm^3)*	*Porosity, P (%)*	*Néel Temp., T_C (^0C)*	*Resonance frequency, f_r (at 10 MHz)*	*Permeability μ_i' (at 100 kHz)*
0.00	900	3.02	42	384	–	33
	1000	3.03	40		–	37
	1100	3.59	35		62	61
	1200	4.33	21		100	102
	1300	4.34	21		–	105
0.05	900	3.07	41	360	–	33
	1000	3.42	39		–	42
	1100	3.90	31		64	63
	1200	4.40	19		145	148
	1300	4.37	19			140
0.10	900	3.2	38	343	–	34
	1000	3.63	36		–	43
	1100	4.09	28		94	93
	1200	4.50	17		150	155
	1300	4.41	17		125	195
0.15	900	3.80	30	326	–	38
	1000	3.81	30		42	44
	1100	4.25	25		102	100
	1200	4.55	14		165	162
	1300	4.50	15		245	248
0.20	900	3.86	20	307	–	41
	1000	3.86	20		45	46
	1100	4.30	18		120	115
	1200	4.60	10		148	180
	1300	4.62	12		262	260
0.25	900	3.80	17	283	–	43
	1000	3.93	7		64	63
	1100	4.36	3		122	120
	1200	4.66	3		227	225
	1300	4.70	5		327	325

Ni, Cu, and Zn oxides are 5.37, 6.72, 6.0, and 5.60 g/cm^3, respectively. The atomic weight of Ni is 58.69, and the atomic weight of Mn is 54.93 amu; which shows that the atomic weight of Ni is heavier than Mn. An increase of Mn content along with decreasing Ni content contributes to reducing porosity resulting in enhancing magnetic induction of the synthesized Nano-crystalline ferrites. It was found that ρ_{th} rises with increasing sintering temperatures decreasing the P % of the ferrites. The total P % can be termed as the intragranular porosity and intergranular porosity. Intragranular porosity, P_{intra} can cause poor magnetic and electrical properties. But intergranular porosity, P_{inter}, depends on particle size (grain size). In our present study, these difficulties are rooted in applying heat treatment within 900–1300 °C. For increasing grain growth, pores are removed in terms of speedily stirring grain boundaries, causing the entrapment of pores in the grains. When the temperature is high, the grains are homogeneous, and empty spaces are lessened; ρ_{bulk} increases, whileρ_{th}, and P % decrease with an increase in Mn content

3.3. Crystallite size

The crystallite sizes were measured by Debye Scherer's formula from the XRD pattern as given in Fig. 2. It was found that the crystallite sizes strongly depend on the Mn concentration, in which crystallite sizes experimentally varied from 20 to 28 nm, which can be attributed based on the coalescence process that decreases the lattice defects and strain. Crystallite size is dependent on the nucleation and growth kinetics during the time of combustion processing. In our prepared ferrites, the crystallite sizes belong to unit

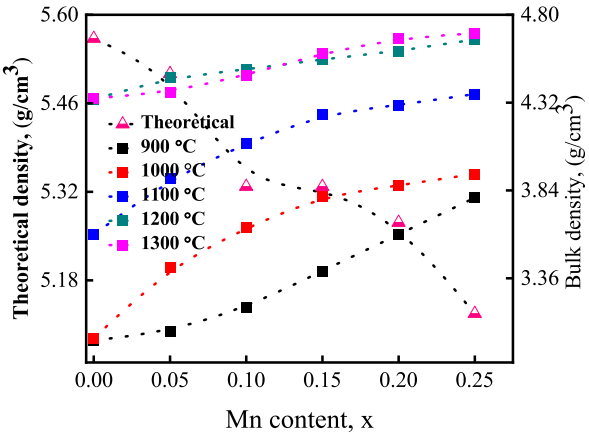

Fig. 4. Variation of bulk density and X-ray density with Mn content for $Ni_{0.50-x}Mn_xCu_{0.15}Zn_{0.35}Fe_2O_4$.

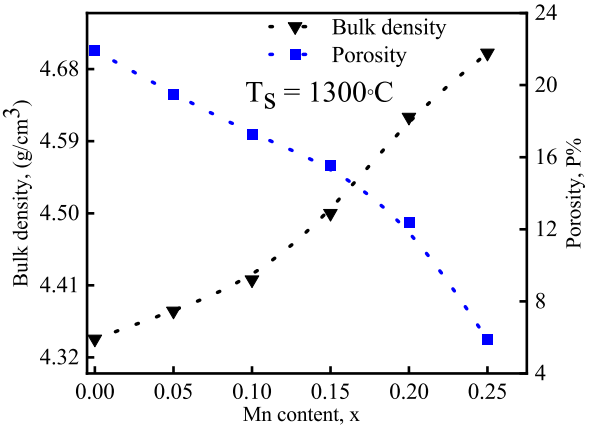

Fig. 5. Variation of density and porosity with Mn content for $Ni_{0.50-x}Mn_xCu_{0.15}\ Zn_{0.35}Fe_2O_4$ sintered at 1300 °C.

cell parameters along with the ionic radius of the incorporation of Mn ions. The uniformly distributed average crystallite size may alter the electronic characteristics of the complex oxides and this dependency revealed for the Nano-crystallites Ni–Mn–Cu–Zn ferrites.

There is a good intimacy between the ionic radius of the incorporation ion and the unit cell, as reported in reference [28,29]. It was demonstrated that when going from the $La_{0.815}$ to $La_{1.0}$ sample increasing the ratio of La/Mn, the unit cell volume increases along with an increase of lattice constant. Surprisingly, bulk density and crystallite size increase, while porosity decreases when Mn concentration increases. So, it turns out that there's a good intimacy among the crystalline size, bulk density, and porosity. Table 1 displays that the values of ρ_{th} are decreased with increasing lattice constant in the Ni–Mn–Cu–Zn systems. It can be attributed to the molecular weight that the molecular weight of each sample was decreased considerably due to the incorporation of Mn concentration. Hence, ρ_{th} is dependent on the lattice parameter along with the molecular weight of the synthesized ferrite samples.

3.4. Morphological study with EDX analysis

3.4.1. Grain size analysis

The morphological structure of as-prepared ash-burnt powders of Ni–Mn–Cu–Zn ferrites without heat treatment is depicted in Fig. 6 by field emission scanning electron micrographs (FESEM). It demonstrated the grains of uniform distribution including the spherical shapes. The linear intercept method was employed to calculate the grain sizes of the synthesized samples, and the average grain sizes for the as-prepared ash-burnt powders varied from 69 to 126 nm. It demonstrated that the average grain sizes increase due to the incorporation of a small amount of Mn content in the synthesized ferrites system. Figs. 7 and 8 demonstrate the scanning electron micrographs that grain size is increasing gradually in which the average grain size varied from ~1.40–2.15 μm when the samples are sintered at 1200 °C, as well as varied from ~2.06–5.30 μm when the prepared samples are sintered at 1300 °C, which is higher compared to the as-prepared powders. The obtained grains from the FESEM show a uniform distribution along with a spherical shape. The average grain size increases, while the porosity decreases. Higher sintering temperatures and longer sintering times may decrease the crystal defects and strain, thereby increasing the grain size. For applying sintering temperature, pores tend to be reduced, and

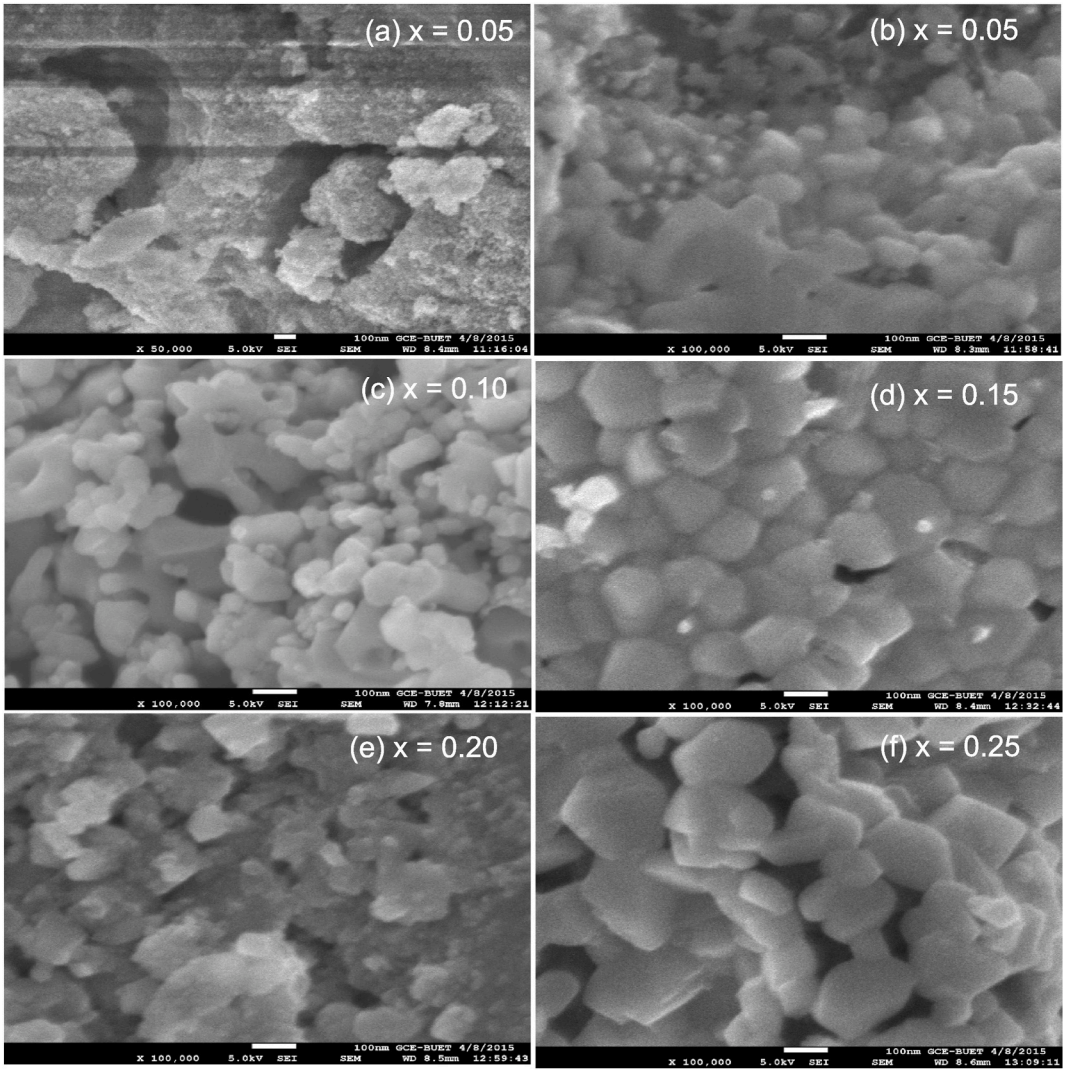

Fig. 6. (a) x = 0.00, **(b)** x = 0.05, **(c)** x = 0.10, **(d)** x = 0.15, **(e)** x = 0.20, and **(f)** x = 0.25 scanning electron micrographs (SEM) of as-prepared powder without heat treatment for $Ni_{0.50-x}Mn_x\ Cu_{0.15}Zn_{0.35}Fe_2O_4$.

average grain size is found to be varied. Besides, the grain sizes considerably depend on the increase of Mn concentration and the decrease of Ni concentration. The average grain size dependency on the Mn concentration is possibly caused by the melting temperature of Mn ∼ 1245 °C and Ni ∼ 1453 °C; indicating that the melting temperature of Ni is higher than that of the melting temperature of Mn. Yan and Johnson [30] described the impact of Mn ions addition on the microstructure of ferrite, noticing that Mn ions work as a maker of grain growth formation as well as even promote dense ferrite materials. Equation (2) can be shown that grain boundary mobility may change grain growth [31] as

$$F = \gamma\ sin\ \theta \times 2\pi r cos\theta, \tag{2}$$

where F indicates the drag force that arises on the grain boundary, γ defines the per unit area-based energy for the particle of radius ,*r*. A grain boundary can run down from the impure atmosphere when driving speed is generous because of the strong driving force on the grain boundary. In this case, drag force may arise due to the objectification of Mn ions in Ni– Mn– Cu– Zn ferrites.

A possible mechanism for promoting grain growth in Cu and Zn co-doped Ni–Mn–Cu–Zn mixed ferrites is the lessening of the impurities along with pores' dragging on the grain boundaries motion [31]. The grain boundary mobility [32] with impurities can be termed as follows-

$$M_b = \frac{D_0 e^{-\frac{(H_D+H_i)}{K\ T}}}{N_b B_0 k\ Tc}, \tag{3}$$

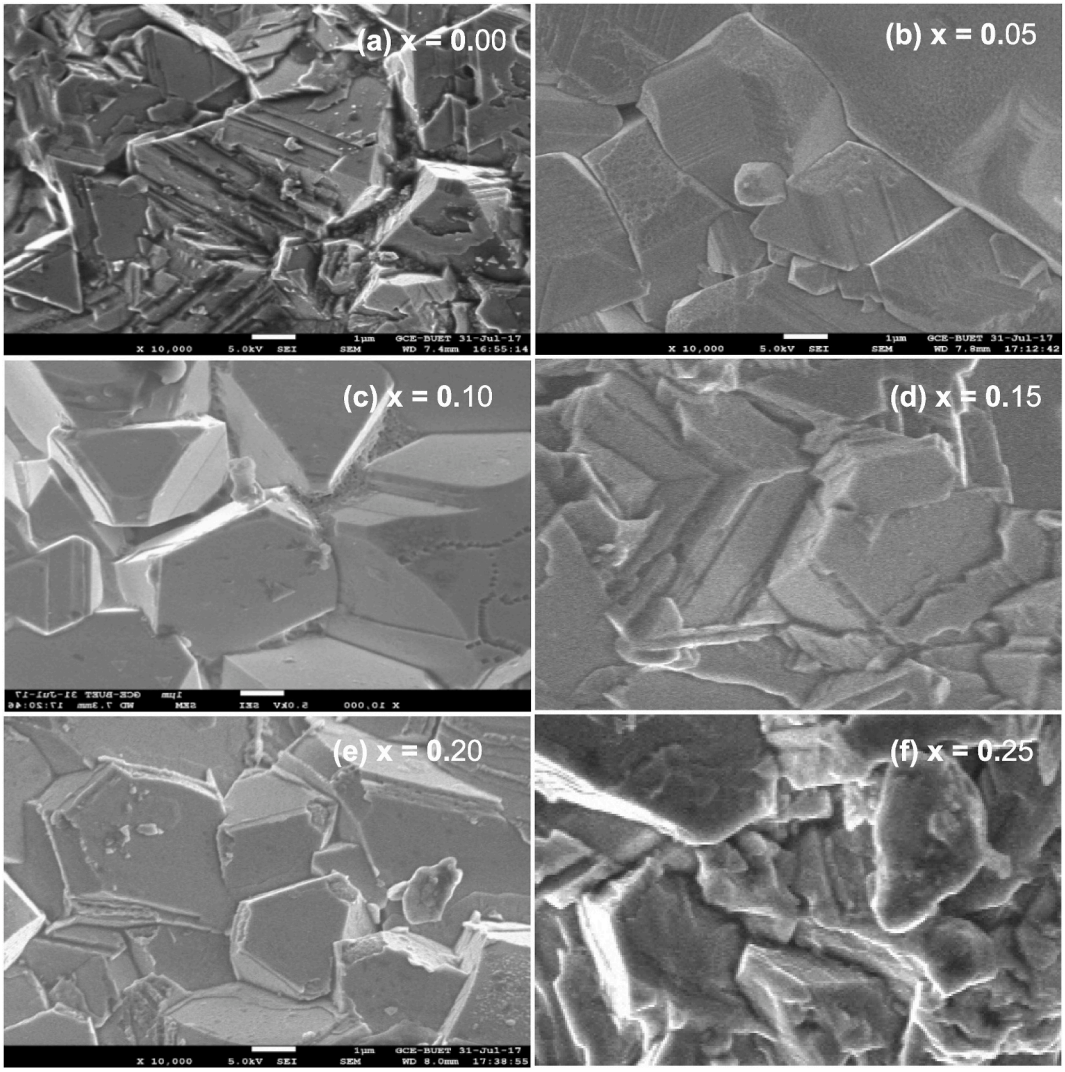

Fig. 7. (a) x = 0.00, **(b)** x = 0.05, **(c)** x = 0.10, **(d)** x = 0.15, **(e)** x = 0.20, and **(f)** x = 0.25 scanning electron micrographs (SEM) of $Ni_{0.5-x}Mn_xCu_{0.15}Zn_{0.35}Fe_2O_4$ as sintered at 1200 °C.

where , $B_0 = e^{-S/KT}$, D_0 is the diffusion coefficient, H_D and H_i are the stimulation enthalpy in the volume diffusion, and the interaction enthalpy for impurity atoms, respectively. N_b defines the adsorption site's number in the grain boundary, K defines the Boltzmann's constant, T is the temperature, and c is the concentration for the volume impurity. Following equation (3), the stimulation enthalpies of impurity atoms to grain boundary movements are responsible for two-enthalpy named impurity diffusions as well as impurity adsorptions. The porosity decreased, and grain size and density increased with increasing sintering temperature. These findings strongly correlate with sintering temperature, porosity, density, and particle size. Grain size affects the electromagnetic properties of ferrites, and the maintenance of microstructures has also a major impact on these characteristics.

3.4.2. EDX analysis, oxygen stoichiometric, and oxygen deficiency

The energy dispersive X-ray (EDX) is a process to determine the sample's elements or characterize its chemical composition. To verify the chemical composition of various $Ni_{0.50-x}Mn_xCu_{0.15}Zn_{0.35}Fe_2O_4$, the EDX spectra were obtained from the FESEM, as shown in Fig. 9. The percentages of elements present along with oxygen stoichiometric are attached in Table 3. The EDX spectra of the samples, which offer the quantitative elemental analysis, were collected at various points. It was obtained that experimental mass (%) and calculating mass (%) were almost comparable.

The EDS analysis is ultimately performed along with SEM analysis. The obtained EDX results are given in Fig. 9 including the results of different points of the spectrum of the samples. The EDX spectrum shows the intensity vs. the energy of the required samples. The qualitative and the quantitative compositional information about the sample are obtained from the EDS study. The qualitative analysis shows the type of elements that exist in the composition i.e., $Ni_{0.50-x}Mn_xCu_{0.15}Zn_{0.35}Fe_2O_4$ (x = 0.00–0.25), and the quantitative

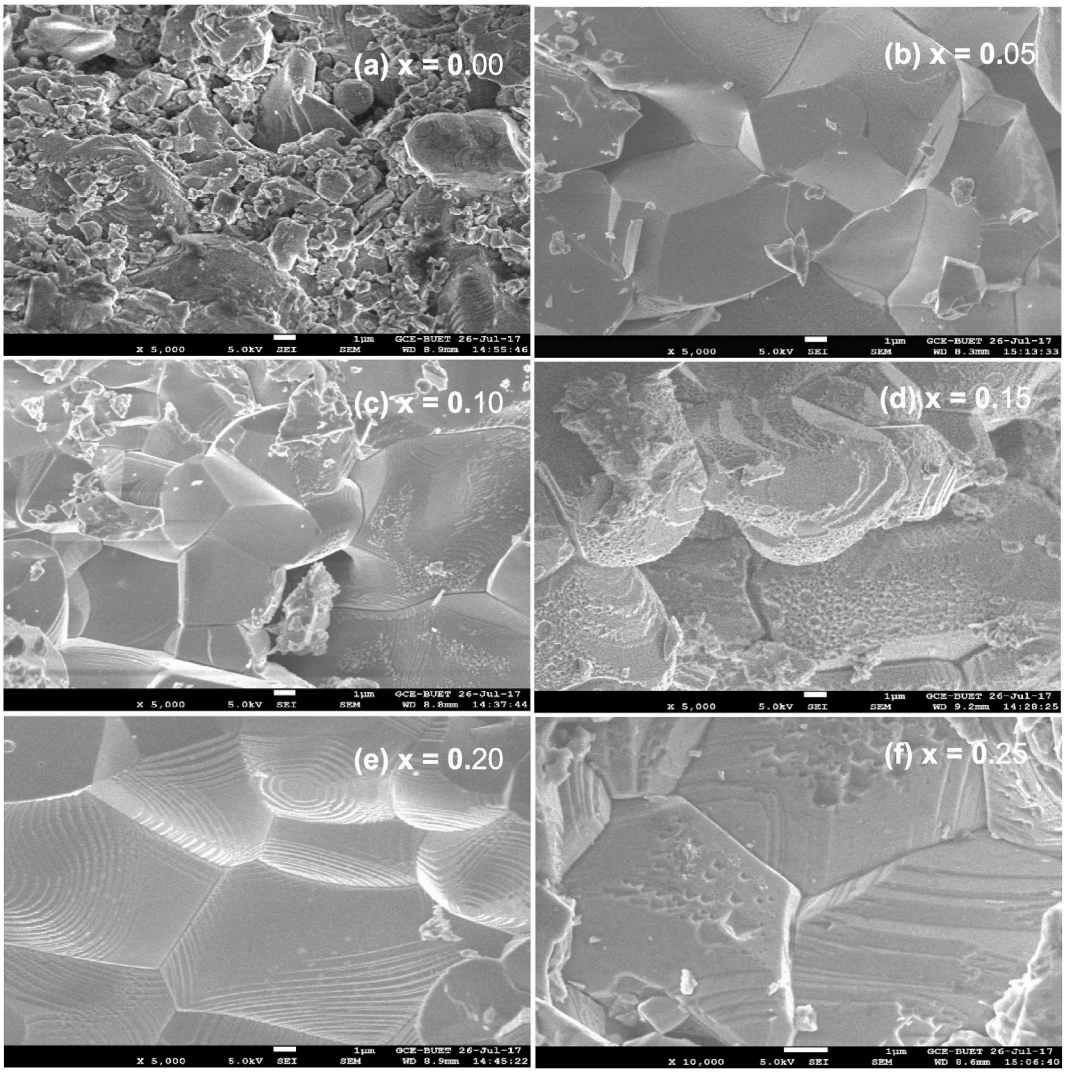

Fig. 8. (a) x = 0.00, **(b)** x = 0.05, **(c)** x = 0.10, **(d)** x = 0.15, **(e)** x = 0.20, and **(f)** x = 0.25 scanning electron micrographs (SEM) of $Ni_{0.5-x}Mn_xCu_{0.15}Zn_{0.35}Fe_2O$ as sintered at 1300 °C.

analysis shows the percentage of elements that exist in the sample in terms of wt. % and atomic %. From the EDS data, oxygen stoichiometric is estimated using equation (4) as follows:

$$O_{stoichiometric} = \frac{O(atom\ \%)}{(Ni + Mn + Cu + Zn + Fe)atom\ \%} \tag{4}$$

Oxygen stoichiometric , $O_{stoichiometric} = \frac{O(atom\%)}{(Ni+Mn+Cu+Zn+Fe)atom\%}$

The perfect value of the oxygen ion stoichiometric of a perfect cubic spinel ferrite is 0.50, which means there are no oxygen vacancies. The oxygen deficiency , δ, can be denoted that the amounts of oxygen atoms are missing from the ideal structure, which this equation can estimate:

$$\delta = 2(0.5 - O_{stoichiometric}) \tag{5}$$

For a perfect spinel ferrite, the oxygen stoichiometric would be zero.

$$\delta = 2\ (0.5 - 0.5)$$

. = 0:

For our prepared sample (x = 0.00 at point 003), when $O_{stoichiometric} = 0.5762$ then the oxygen deficiency are calculated from equation (5) as

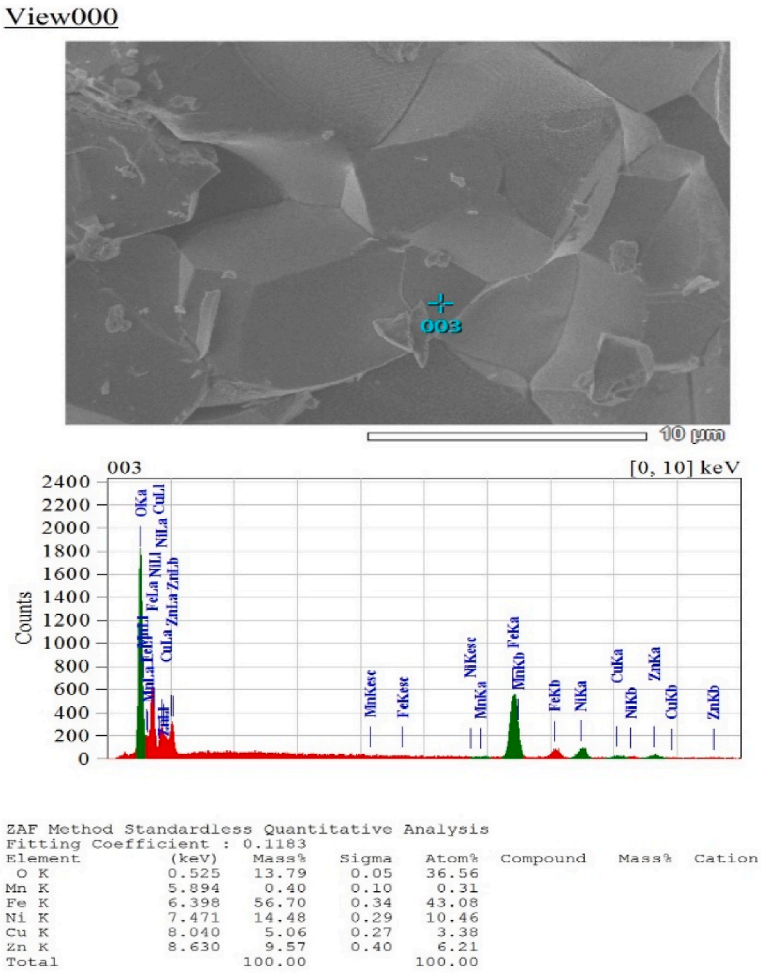

Oxygen stoichiometry deficiency calculation from EDS spectra

Elements	Experimental Mass %	Experimental Atom %	Calculating Mass %	Oxygen stoichiometric $O_{stoichiomeric}$
O	13.79	36.56	5.52	
Mn	0.40	0.31	0.00	
Fe	56.70	43.08	69.78	+ 0.5762
Ni	14.48	10.46	12.58	
Cu	5.06	3.38	3.13	
Zn	9.57	6.21	8.99	
Total	100	100	100	

Fig. 9. EDS spectra of point (003) of $Ni_{0.50-x}Mn_xCu_{0.15}Zn_{0.35}Fe_2O_4$ sintered at 1300 °C for x = 0.00.

$\delta = 2(0.5 - O_{stoichiometric})$

$= 2(0.5 - 0.5762)$

Table 3
Oxygen stoichiometric and oxygen deficiency calculation from EDS spectra.

Contents	Spectrum at Point	Oxygen Stoichiometric, $O_{stoichiometric}$	Oxygen Deficiency, $\delta = 2\ (0.5 - O_{stoichiometric})$	Oxygen Deficit/Excess $= (4 - \delta)$
x = 0.00	Point (001)	0.3812	+0.2376	3.7624
	Point (002)	0.5857	−0.1714	4.1714
	Point (003)	0.5762	−0.1524	4.1524
x = 0.05	Point (001)	0.6155	−0.2310	4.2310
	Point (002)	0.6448	−0.2896	4.2896
	Point (003)	0.5662	−0.1324	4.1324
x = 0.10	Point (001)	0.1667	+0.6670	3.7624
	Point (002)	0.4475	+0.1050	3.333
	Point (003)	0.6181	−0.2362	4.2362

Or, $\delta = -0.1524$
Then the oxygen content becomes $= (4 - O_{stoichiometric})$
. = 4 − (− 0.1524):

. = : 4.1524

For a perfect cubic spinel ferrite, oxygen stoichiometric approaches 0.5, and then δ becomes zero. From the above equation, δ values are calculated for some compositions as given in Table 3. The values of δ vary slightly for different points of the SEM micrographs. These results agree with previously reported results [8,9]. Hence, the samples for x = 0.00 to 0.25 can be predicted to be almost ideal since δ is nearly equal to zero [9]. This indicates that the citric acid-aided sol-gel auto-combustion route is excellent for producing nano-particles of Ni–Mn–Cu–Zn ferrites.

Additional oxygen and oxygen deficiency for 3d-metallic elements can cause an increase or decrease in the oxidation degree.

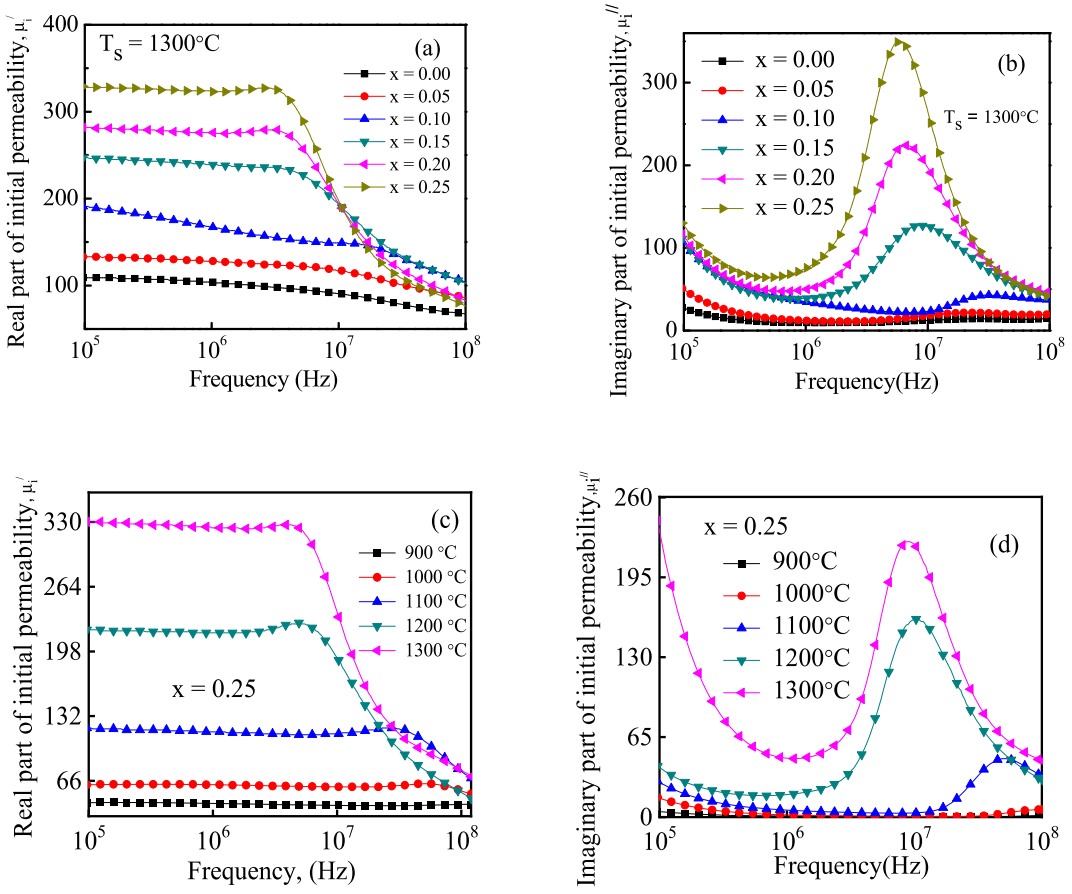

Fig. 10. (a) Real and **(b)** imaginary permeability spectra for typical samples sintered at 1300 °C and **(c)** The real and **(d)** imaginary permeability spectra for x = 0.25 sintered at 900, 1000, 1100, 1200, and 1300 °C in air.

Changing the charge state of 3d-metallic elements resulting in oxygen deficiency may alter the electromagnetic and optical characteristics of the ferrite materials. The unit cell parameter belongs to the , δ, and it may impact on δ[33,34].

In our present samples, oxygen content excess and/or deficit vary from ~4.15 to 3.76. However, the value of $O_{stoichiometric}$ can deviate from 0.5 due to various factors, such as the incorporation of Fe instead of Cu and Zn, the oxidation or reduction of the metal cations, and the formation of oxygen vacancies or interstitials. The deviation of δ from 0 may impact the functional features of the nanocrystalline spinel ferrites, such as the lattice parameter, permeability, coercivity, saturation magnetization, Curie temperature, band gap, and optical absorption.

According to some research articles [35–37], a lower oxygen stoichiometry can increase the permeability and the saturation magnetization of this spinel type of ferrite, as it enhances the magnetic exchange interactions and also magnetic anisotropy constants Besides these, the précised complex initial permeability, saturation magnetization, and coercivity depend on other factors, such as the cation distribution of the nominal composition, the synthesis method, grain size and the applied heat treatment i.e. sintering temperature.

3.5. Magnetic property

3.5.1. Initial permeability

Permeability is an essential key factor in evaluating a material's magnetic properties that defines the material's response to the magnetic field. The ratio of magnetic field induction, *dB* to the magnetic field intensity, *dH* is termed the permeability of a ferrite material. For modern transformers or interference suppression components, inductance is determined through the following relation:

Incremental magnetic permeability , $\mu_A = \frac{1}{\mu_0}\ \frac{dB}{dH}$,

where, μ_0 directs the permeability of free space. When the applied magnetic field is tiny; indicating the most zero value, however, the proportion of magnetic field induction to the magnetic field intensity is defined as initial permeability given by this equation [38]:

$$\mu_i = \frac{1}{\mu_0}\ \lim_{H\to 0}\frac{\Delta B}{\Delta H}$$

μ_i is represented by a slope of the linear line under vanishingly low fields, but the incremental permeability describes the amplitude permeability within the complete hysteresis loop.

Initial permeability depends on the microstructure, temperature (annealing and sintering), magnetization, stress, and several other factors. Our present study discussed how permeability depends on the sintering temperature, particle size, domain wall energy, and anisotropy constant. The compositional dependency of the complicated initial permeability spectra for different Ni–Mn–Cu–Zn ferrites sintered at 1300 °C is shown in Fig. 10(a and b). The sintering temperatures dependent permeability spectra for $Ni_{0.25}Mn_{0.25}Cu_{0.15}Zn_{0.35}Fe_2O_4$ are plotted in Fig. 10(c and d). For substituting high spin Mn^{2+} concentration in the Ni–Mn–Cu–Zn ferrite system, initial permeability , $\mu_i^{'}$ is enhanced. This outcome can be attributed to the cation redistribution.

The possible cation distribution for $Ni_{0.50\text{-}x}Mn_xCu_{0.15}Zn_{0.35}Fe_2O_4$ can be expressed as

$$(Zn_{0.35}Mn_{0.8x}Fe_{0.65\text{-}0.8x})\ [Mn_{0.2x}Ni_{0.50\text{-}}xCu0_{.15}Fe_{1.35+0.8x}]\ O_4 \quad (6)$$

Hence, net magnetization, $M_{net} = [M]_B - (M)_A$

or

$$M_{net} = (3x + 4.5)\mu_B \quad (7)$$

The squared bracket term defines the octahedral B-site, while the first term defines the tetrahedral A-site. The net magnetization, M_{net} of the produced samples the B-site and the A-site are expressed as the variables $[M]_B$ and $(M)_A$, respectively. According to the evidence of the articles, about 80% of manganese ions are found in the A-site, while the rest of 20 % are occupied in the B-site [39]. Although Fe and Mn ions may occupy both the sites of A and B, they prefer the B- and A-site, independently. Ni, Cu, and Zn ions inhabit the octahedral site, whereas Fe and Mn ions prefer the tetrahedral site [40]. For the addition of various ions in the synthesized composition, several iron ions migrate from the A-site to the B- site due to the site choice. When Mn^{2+} is hosted at the expense of Ni^{2+}, increasing the content of Fe ions at the octahedral site then Fe ions tend to be shifted to increase M_{net} The Bohr magneton, μ_B of Mn is $5\mu_B$ and Ni is $2\mu_B$; consequently, with a tiny quantity of manganese content in the samples then μ_B of the octahedral sub-lattice increases. However, the magnetic moment of the A sub-lattice is constant as Mn concentration rises, whereas the magnetic moment of the B sub-lattice rises. We can see from equations (6) and (7) that when a small amount of Mn ions is incorporated in $Ni_{0.50\text{-}x}Mn_{x\text{-}}Cu_{0.15}Zn_{0.35}Fe_2O_4$, then M_{net} increases with increasing Mn showing the decrease of Ni content.

The polycrystalline ferrite's permeability is associated with two different influencing factors, which are called the magnetizing factors named (i) spin rotation or intrinsic rotational susceptibility, χ_{spin} and (ii) domain wall motion or domain wall susceptibility, χ_ω [41,42], that is termed as

$$\mu_i = 1 + \chi_\omega + \chi_{spin}, \quad (8)$$

$$\text{Domain wall susceptibility}, \chi_\omega = \frac{3\pi M_{net}^2 \tau}{4\gamma}, \quad (9)$$

$$\text{and spin rotation, } \chi_{spin} = \frac{2\pi M_{net}^2}{K_u}, \tag{10}$$

where M_s indicates saturation magnetization, K_u defines the anisotropy constants, τ is the average grain diameter, and γ indicates the energy of the domain wall.

From equations (8)–(10) it can be concluded that the spin rotation along with the domain wall motion is an important parameter in enhancing $\mu_i^{'}$. The $\mu_i^{'}$ is the factor to express the stored energy. The various parameters, which contribute to $\mu_i^{'}$ are given by

$$\text{The real part of initial permeability, } \mu_i^{'} = \frac{3\tau\mu_0 M_s^2}{16\gamma}, \tag{11}$$

From equation (11) it is seen that there are excellent relationships among domain wall motion (domain wall susceptibility), net magnetization, particle size, and domain wall energy. For incorporating a small amount of Mn ions in $Ni_{0.50-x}Mn_xCu_{0.15}Zn_{0.35}Fe_2O_4$, both saturation magnetization and grain diameter are increased, and anisotropy constant is also decreased, its eventually $\mu_i^{'}$ increases with an increase of manganese ions along with the reduction of nickel ions as presented the$\mu_i^{'}$ value in Table 2. It was revealed that $Ni_{0.25}Mn_{0.25}Cu_{0.15}Zn_{0.35}Fe_2O_4$ composition had a greater permeability of about 315. It was demonstrated that $\mu_i^{'}$ is increased with the enhancement of heat treatment for all ferrite samples. The 25 % manganese substituted composition exhibits the highest permeability of all samples when sintered at 1300 °C, in which the surface morphological structure is uniform with enlarged grain distribution. In addition, inserting Mn ions rather than Ni ions increases the grain size and saturation magnetization of the synthesized ferrite materials, resulting in the enhancement of χ_ω and χ_{spin} to increase the $\mu_i^{'}$.The $\mu_i^{'}$ remains constant up to a certain frequency, which is called critical frequency or the resonance frequency , f_r. For decreasing Ni concentration in the Ni–Mn–Cu–Zn ferrite system, then f_r tends to be enhanced due to the certain sintering temperature, T_s as f_r values given in Table 2. $\mu_i^{'}$ value for all synthesized samples is investigated and is remains constant below f_r. It was found that there was a sharply decreased trend of $\mu_i^{'}$ and an increased trend of $\mu_i^{''}$ above f_r. It was noted that f_r and $\mu_i^{'}$ are inversely proportional to each other, which confirms Snoek's relation, $f_r\mu_i^{'}$ = constant. It is observed that for various $Ni_{0.50-x}Mn_xCu_{0.15}Zn_{0.35}Fe_2O_4$ Both $\mu_i^{'}$ and ρ_{Bulk} are increased with increasing.T_s for various $Ni_{0.50-x}Mn_xCu_{0.15}Zn_{0.35}Fe_2O_4$. Nevertheless, $\mu_i^{'}$ of all produced ferrite samples is dependent on the density of the nominal compositions.

3.5.2. Relative quality factor

The variation of relative quality factor (RQF or Q-factor) Vs. frequency plot, as presented in Fig. 11, it was observed that the Q-factor tends to be raised within the limit of a certain frequency and reached a resonance peak after that started to fall as frequency increased even higher. The Q-factor is observed to reduce up to 60 MHz, in which the loss tangent displays a low value before rising quickly. The magnetic loss tangent can be ascribed to the several imperfections of the domain [43]. The loss is initiated by the domain wall motion that delays behind the applied alternating magnetic field. This magnetic loss is caused during the resonance frequency in which the frequency-dependent permeability tends to be decreased. The ferromagnetic resonance within the domains is responsible for this occurrence. At the resonance frequency, the maximum amount of energy goes to the lattice from the applied field, which causes a prompt decreased trend in the RQF factor. With an x value of 0.25, the sample $Ni_{0.25}Mn_{0.25}Cu_{0.15}Zn_{0.35}Fe_2O_4$ has the highest Q-factor at about 3800 across all sintering temps. The magnetic loss factor increases with rising temperature when the frequency is ~1 MHz. In addition, it has been found that magnetic loss tangent reduces with the enhancement of manganese content. For $Ni_{0.30}Mn_{0.20}Cu_{0.15}Zn_{0.35}Fe_2O_4$ (x = 0.20) and $Ni_{0.25}Mn_{0.25}Cu_{0.15}Zn_{0.35}Fe_2O_4$ (x = 0.25), *tan* δ_m also increases promptly when the frequency is around 10 MHz. A resonance peak is shown to fall quickly over the improvement of *tan* δ_m. It is predicted that the phase

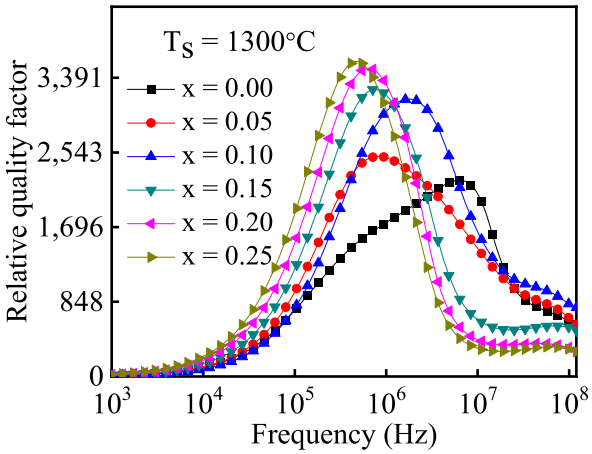

Fig. 11. Variation of Q-factor with frequency for typical samples sintered at 1300 °C.

laggings among the domains and applied fields are more important. Higher sintering temperatures are unfavorable for minimizing magnetic loss, but the incorporation of magnetic ions is also effective in doing so. The proportion of $\mu_i^{'}$ and $\mu_i^{''}$ represents the magnetic loss tangent in the synthesized samples, which is the measure of the inadequacy of the Ni–Mn–Cu–Zn ferrite system, thus, *tan* δ_m factor ought to be as low as possible. The magnetic loss tangent can be of the form

$$tan\ \delta_m = tan\ \delta_h + tan\ \delta_e + tan\ \delta_r, \tag{12}$$

where *tan* δ_m terms the magnetic loss tangent, which roots the phase-shifting. It is found from equation (12) that *tan* δ_m is also classified as three portions named (a)hysteresis losses, *tan* δ_h, (b)eddy current losses, *tan* δ_e, and (c)residual losses, *tan* δ_r. The $\mu_i^{'}$ is interrelated to the low-applied field, which *tan* δ_h may vanish at a very small field intensity. Therefore, at a very small field, the rest part of *tan* δ_m belongs to the *tan* δ_e and *tan* δ_r. The *tan* δ_r does not depend on frequency, and *tan* δ_e is increased with frequency, which can be neglected at very low frequencies. *tan* δ_e is defined as

$$P_{eddy} = \frac{f^2}{\rho}, \tag{13}$$

where P_{eddy} signs the per unit volume-based energy loss, as well as ρ defines the resistivity [44]. equation (13) makes a correlation among the frequency, resistivity, and energy loss per unit volume of the prepared materials. Frequency should be as high as possible to remain *tan* δ_e constant; hence, ρ of the ferrite materials must be equal to the square of the frequency. The eddy current, which is not a problematic issue in the Ni–Mn–Cu–Zn ferrite system till high frequency is considered, as ferrite-based material has a very high resistivity of the order of $\sim 10^5 - 10^8\ \Omega$cm. The mixed spinel-typed ferrites belong to the surface morphology, which contains grains as well as grain boundaries. Grains may behave as conductors containing a very low resistance, but grain boundaries may behave as insulators having high resistance. Thicker grain boundaries are favored to boost resistance.

3.5.3. Temperature-dependent permeability and Néel temperature

To analyze the temperature dependency $\mu_i^{'}$ and Néel temperature, T_C a graph is plotted as shown in Fig. 12 having a fixed frequency (100 kHz) by a sinusoidal wave. It is obtained from the plot of $\mu_i^{'}$ Vs. T that there was an increased trend in $\mu_i^{'}$ with temperature showing a temperature coefficient of $\mu_i^{'}$ as ($\mu_i^{'}$/dT) and raising to the peak values near T_C and then suddenly making a sharp drop at T_C. With increasing temperature, a severe dropping in $\mu_i^{'}$ indicates the prepared samples' single-phase formation and reveals the uniformity of the synthesized ferrites [45], which can be attributed to the X-ray diffraction. T_C is calculated by graphing a tangent for a curve at the rapid reduction of $\mu_i^{'}$. From Fig. 12, it is investigated that $\mu_i^{'}$ is dependent on the incorporation of Mn substitution. Thus, $\mu_i^{'}$ is increased with the enhancement of manganese concentration and with the reduction of nickel concentration. $\mu_i^{'}$ is dependent on oxygen stoichiometry,$O_{stoich.}$ [46], average grain size, nominal composition, crystal imperfections as impurity content, magneto crystalline anisotropy, porosity, and surface morphology. It is demonstrated that $\mu_i^{'}$ is enhanced gradually with increased grain diameter, and oxygen stoichiometric ratio but falls with increasing P % and K_u [47]. Domain wall motion contributes to the initial permeability but is a minor outcome due to spin rotation [48]. The first increased trend in $\mu_i^{'}$ defines the stoichiometric $O_{stoich.}$ and K_u effect. K_u is so small for ferrite materials in which K_u for Ni–Zn ferrite is -1.7×10^3 J/m^3 and it is -0.2×10^3 J/m^3 for Mn–Zn ferrites [49] that gives us information about the incorporation of manganese ions instead of nickel ions. The anisotropy constant is reduced when a small amount of Mn ions are incorporated into this ferrite system. Therefore, $\mu_i^{'}$ is found to be increased for a smaller value of Mn content. T_C defines the transition temperature above which the ferrimagnetic ferrite materials converted into a paramagnetic phase giving an idea of how much energy is required to break down the long-range ordering in the synthesized ferrite samples. From Fig. 12 it was observed that T_C decreased with increasing Mn ions, T_C for various compositions as tabulated in Table 2. The reduction of T_C can be ascribed to the exchange interaction among the ions of the nominal composition as well as by the variation of $r_{variant}$. For the expansion of the unit cell along with increasing lattice constant, which may impact the exchange interaction and consequently a falling trend of T_C has arisen with increasing Mn ions in the composition. In this composition, iron ions as a ferromagnetic have been substituted by manganese ions as a paramagnetic for each step of incorporation; it's eventually, a shrinkage in the concentration of magnetic ions and the magnetic moment of the sub-lattices. A reduction of T_C can also be attributed to the weakening of the A-B exchange interaction. An increase in distance can explain the hopping length, L, as shown in Fig. 13, between the magnetic ions of the A-site (L_A) and the B-site (L_B). For increasing Mn content L_A is increased, while L_B is decreased with enhanced lattice parameters. This variation in hopping lengths can be attributed to the reduction of T_C and the increase of lattice parameters with the improvement of manganese content in the investigated ferrites system. From Fig. 13, it was obtained that the perpendicular falling of $\mu_i^{'}$ at T_C exhibits the degree of homogeneousness in the synthesized ferrite materials [50]. Accordingly, the prepared sample has exposed an exceptional degree of uniformity. With an increase in temperature, $\mu_i^{'}$ turns to be smaller, which does not depend on temperature i.e. demonstrates the characteristics of paramagnetic. Some peaks formed near T_C are termed the 'Hopkinson' peak [51], which indicates the single domain present in the ferrite materials. The discrepancy in $\mu_i^{'}$ originated mainly due to K_u. The anisotropy constant ,K_u, varies significantly with temperature. On heating, as K_u decreases faster than magnetization, then$\mu_i^{'}$ increases rapidly with temperature, which becomes infinitive under the T_C, and then a sharp falling from the ferrimagnetic to the paramagnetic phase.

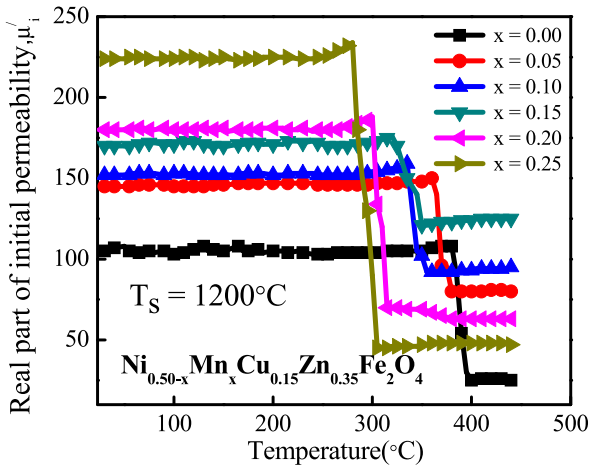

Fig. 12. Temperature dependence for various $Ni_{0.50-x}Mn_xCu_{0.15}Zn_{0.35}Fe_2O_4$ samples as sintered at 1200 °C.

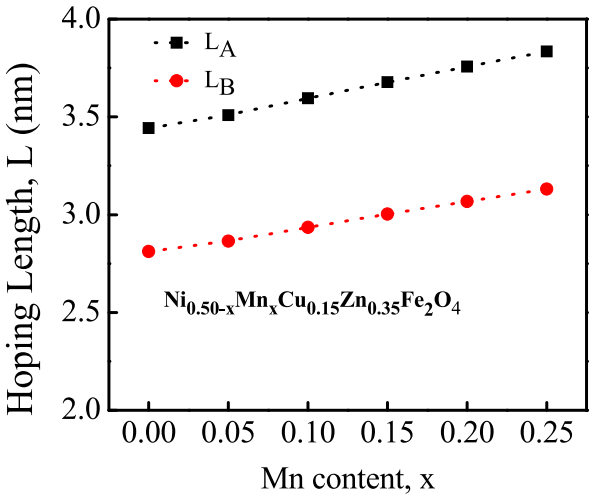

Fig. 13. Plot of hopping length (L) of A-site and B-site (L_A and L_B) Vs. Mn content for typical samples.

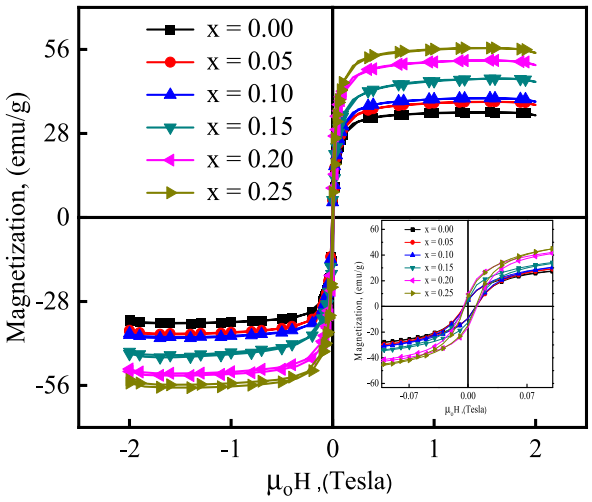

Fig. 14. Magnetization Vs. the applied magnetic field plot for as-prepared powder of $Ni_{0.50-x}Mn_xCu_{0.15}Zn_{0.35}Fe_2O_4$.

3.5.4. DC magnetization and coercivity

The magnetization Vs. the applied magnetic field, M − H, loop at room temperature was shown in Fig. 14. The variations in M_s for the prepared sample have been studied; in which this variation in M_s is overcome depending on the cation distribution as well as exchange interactions in-between Fe^{2+} ions and in-between Mn^{2+} ions at A-site and B-site. Due to hosting manganese content instead of nickel content, hence the movement of iron ions is accomplished from A to the B-site due to the site preference for various ions. As a result, M_{net} of the B sub-lattice is enhanced with increasing Mn concentration. Magnetization for all samples rises gradually with an increase of applied magnetic field up to the value of ~0.8T, then M_s is occurred. It was found that all compositions exhibit the ferrimagnetic state at room temperature. M_s value for all samples is listed in Table 1, showing that an increase of manganese content M_s is increased. The higher the Mn content the higher the M_s. Fig. 15 shows the variation in M_s and H_c; in which M_s varied ~34.31–54.95 emu/g, while H_c dropped from ~5.71 to 5.20 kA/m. It was demonstrated that at 0% Mn content exhibits the highest H_c and the lowest M_s. Coercivity, H_c, which may be influenced by surface morphology, magneto crystalline anisotropy, micro-strain, shape anisotropy, and oxygen deficiency [8,9,52]. H_c is reduced by decreasing Ni content, and H_c is increased by increasing Mn ions. These activities could be connected to the property of porosity. The porosity can affect the magnetization process, in which pores for crystal imperfections may act as an initiator of the demagnetizing field. For decreasing porosity, a high magnetic applied field is to be required to initiate the domain wall, therefore, H_c is decreased. Coercivity, somehow, is concerned with the anisotropy constant. Following the one-ion model, which correlates between the iron ions (Fe^{2+}) and the ferrites' magneto crystalline anisotropy constants k_u [53–56]. In this present study, it was found that due to an increase of Mn^{2+} content instead of Ni^{2+} content k_u is decreased; hence H_c is decreased. M_s is connected to the coercivity, H_c via Brown's relation [57,58]. Brown's relationship is written as

$$H_c = \frac{2k_u}{\mu_0 M_s} \tag{14}$$

$$H_c = \frac{0.96k_u}{M_s} \tag{15}$$

where k_u defines the magneto crystalline anisotropic constants, μ_0 terms the permeability of free space. Following these equations (14) and (15), H_c and k_u are directly proportional to each other, and H_c and M_s are inversely proportional to each other; therefore, it's a good similarity with our experimental results, as pictured in Fig. 15 and tabulated in Table 1. H_c decreases sharply with an increase of manganese concentration, which is described by the quenched orbital angular momentum of Mn.

4. Conclusions

This present research work describes the impact of manganese incorporation on the structure, surface morphology, and functional characteristics of the Ni–Mn–Cu–Zn mixed ferrites. Introducing high-spin Mn ions into the spinel-typed lattice leads to the increase of average grain size within ~20–28 nm for as-prepared powders, ~1.40–2.15 μm when the samples are sintered at 1200 °C, and ~2.06–5.30 μm when the samples are sintered at1300 °C; for that reason, it can be noted that Mn^{2+} acts as a grain growth accelerator. In contrast, bulk density increased from ~3.02 to 4.70 g/cm^3, and initial permeability ranged from 105 to 325. Higher sintering temperatures and longer sintering times may decrease the crystal defects and strain, thereby increasing the particle size. The relative quality factor for the 25% Mn substituted composition displayed the highest value of ~3800. The temperature-dependent permeability graph shows that the Néel temperature decreases from ~384 to 283 °C as Mn content rises, a sharp transition also reveals an excellent degree of homogeneity of the samples. Above Néel temperature initial permeability turns into the smaller value exhibiting the paramagnetic behavior. The $Ni_{0.25}Mn_{0.25}Cu_{0.15}Zn_{0.35}Fe_2O_4$ sample shows the highest permeability, saturation magnetization, quality

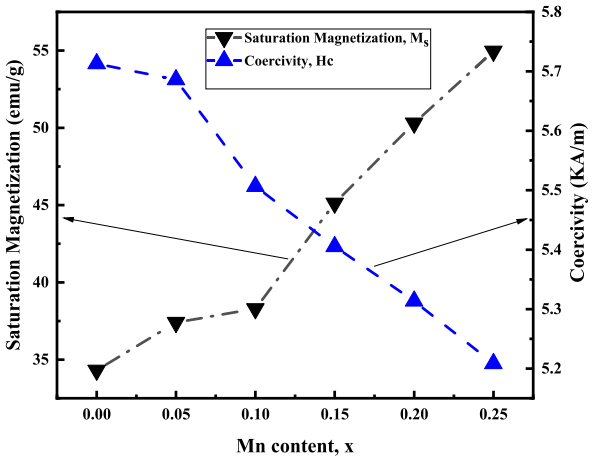

Fig. 15. Variation of saturation magnetization and coercivity with Mn content, x.

factor, lowest coercivity, and Néel temperature among all the compositions studied here. The prepared sample would be a great fit to use up to the frequency range ~10 MHz than other substituted ferrites. Our prepared Ni–Mn–Cu–Zn ferrites show low coercivity and high permeability characteristics and may be employed for medical purposes such as cancer treatment. Lastly, it can be decided that the high-spin Mn substitution yields better nanomaterials with improved physical and magnetic properties for the fabrication of multifunctional electronic devices.

Data availability statement

The authors confirm that the data supporting the study's findings are accessible within the articles. The corresponding author will provide the raw data supporting the study's findings upon a reasonable request.

CRediT authorship contribution statement

Abdul Ahad: Writing – original draft, Methodology, Investigation. **A. K. M. Akther Hossain:** Supervision, Fund acquisition, manuscript revision and interpretation.

Declaration of competing interest

The authors declare that they have no known competing financial interests or personal relationships that could have appeared to influence the work reported in this paper.

Acknowledgments

This work has been financially supported by the CASR, Grant No 345(60) of the Bangladesh University of Engineering & Technology (BUET), Dhaka, Bangladesh.

References

[1] A.A. Momin, R. Parvin, Hossain A. K. M. Akther, Structural, morphological and magnetic properties variation of nickel-manganese ferrites with lithium substitution, J. Magn. Magn Mater. 423 (2017) 124, https://doi.org/10.1016/j.jmmm.2016.09.078.
[2] D.A. Vinnik, V.E. Zhivulin, D.P. Sherstyuk, A.Yu Starikov, P.A. Zezyulina, S.A. Gudkova, D.A. Zherebtsov, K.N. Rozanov, S.V. Trukhanov, K.A. Astapovich, V. A. Turchenko, A.S.B. Sombra, D. Zhou, R.B. Jotania, C. Singh, A.V. Trukhanov, Electromagnetic properties of zinc-nickel ferrites in frequency range of 0.05-10 GHz, Mater, Today Chem 20 (2021) 100460, https://doi.org/10.1016/j.mtchem.2021.100460.
[3] D.A. Vinnik, V.E. Zhivulin, D.P. Sherstyuk, A.Yu Starikov, P.A. Zezyulina, S.A. Gudkova, D.A. Zherebtsov, K.N. Rozanov, S.V. Trukhanov, K.A. Astapovich, A.S. B. Sombra, D. Zhou, R.B. Jotania, C. Singh, A.V. Trukhanov, Ni substitution effect on the structure, magnetization, resistivity, and permeability of zinc ferrites, J. Mater. Chem. C 9 (2021) 5425–5436, https://doi.org/10.1039/D0TC05692H.
[4] A.V. Trukhanov, V.G. Kostishyn, L.V. Panina, V.V. Korovushkin, V.A. Turchenko, P. Thakur, A. Thakur, Y. Yang, D.A. Vinnik, E.S. Yakovenko, L.Yu Matzui, E. L. Trukhanova, S.V. Trukhanov, Control of electromagnetic properties in substituted M-type hexagonal ferrites, J. Alloys Compd. 754 (2018) 247–256, https://doi.org/10.1016/j.jallcom.2018.04.150.
[5] V. Turchenko, A. Trukhanov, S. Trukhanov, M. Balasoiu, N. Lupu, Correlation of crystalline and magnetic structures of barium ferrites with dual ferroic properties, J. Magn. Magn Mater. 477 (2019) 9–16, https://doi.org/10.1016/j.jmmm.2018.12.101.
[6] V.E. Zhivulin, E.A. Trofimov, O.V. Zaitseva, D.P. Sherstyuk, N.A. Cherkasova, S.V. Taskaev, D.A. Vinnik, YuA. Alekhina, N.S. Perov, K.C.B. Naidu, H.I. Elsaeedy, M.U. Khandaker, D.I. Tishkevich, T.I. Zubar, A.V. Trukhanov, S.V. Trukhanov, Preparation, phase stability and magnetization behavior of high entropy hexaferrite, iScience 26 (2023) 107077, https://doi.org/10.1016/j.isci.2023.107077.
[7] V.T. Zaspalis, V. Tsakaloudi, M. Kolenbrander, The effect of dopant on the incremental permeability of MnZn ferrites, J. Magn. Magn Mater. 313 (2007) 29–36, https://doi.org/10.1016/j.jmmm.2006.11.210.
[8] P.N. Lisboha-Filho, M. Bahout, P. Barahona, C. Moure, O. PenaV, T. Zaspalis, Oxygen stoichiometry effects in spinel-type $NiMn_2O_{4-8}$ samples,, J. Phys. Chem. Solid. 71 (2010) 1669, https://doi.org/10.1016/j.jpcs.2005.03.001.
[9] R.E. El-Shater, H. El Shimy, S.A. Saafan, M.A. Darwish, D. Zhou, K.C.B. Naidu, M.U. Khandaker, Z. Mahmoud, A.V. Trukhanov, S.V. Trukhanov, F. Fakhry, Fabrication of doped ferrites and exploration of its structure and magnetic behavior, Mater. Adv. 4 (2023) 2794–2810, https://doi.org/10.1039/d3ma00105a.
[10] Alexandre R. Bueno, L. Maria, Gregori, C.S. Maria, No Brega, Effect of Mn substitution on the microstructure and magnetic properties of $Ni_{0.50-x}Zn_{0.50-x}Mn_{2x}Fe_2O_4$ ferrite prepared by the citrate–nitrate precursor method, J. Mater. Chem. Phys. 105 (2007) 229, https://doi.org/10.1016/j.matchemphys.2007.04.047.
[11] B.V. Bhise, M.B. Dongare, S.A. Patil, et al., X-ray infrared and magnetization studies on Mn substituted Ni-Zn ferrites, J. Mater. Sci. Lett. 10 (1991) 922–924, https://doi.org/10.1007/bf00724783.
[12] A.A. Sattar, H.M. El-Sayed, K.M. El-Shokrofy, M.M. El-Tabey, Effect of manganese substitution on the magnetic properties of nickel-zinc ferrite, J. Mater. Eng. Perform. 14 (2005) 99, https://doi.org/10.1361/10599490522185.
[13] E. Shirsath Sagar, B.G. Toksha, R.H. Kadam, S.M. Patange, D.R. Mane, Doping effect of Mn^{2+} on the magnetic behavior in Ni-Zn ferrite nanoparticles prepared by sol-gel auto combustion, J. Phys. Chem. Solid. 71 (2010) 1669, https://doi.org/10.1016/j.jpcs.2010.08.016.
[14] TA Wani, G Suresh, R Masrour, KM Batoo, A Rasool A structural, morphological, optical and magnetic study of nickel-substituted zinc (Ni-Zn) ferrite nanoparticles synthesized via glycine assisted gel auto combustion synthesis route, Mater. Chem. Phys. 307, 128169. https://doi.org/10.1016/j.matchemphys.2023.128169.
[15] V. Jagadeesha Angadi, K M Batoo, S Hussain, S O Manjunatha, S Wang, Synthesis and study of transition metal (Co, Cu, and Ni) substituted ferrites for humidity sensor applications J. Mater. Sci. Mater. Electron., 34 (4), 301. https://doi.org/10.1007/s10854-022-09694-5.
[16] Khalid Mujasam Batoo, Muhammad Hadi, Ritesh Verma, Ankush Chauhan, Rajesh, Improved microwave absorption and EMI shielding properties of Ba-doped Co-Zn ferrite, Ceram. Int. 48 (3), 3328-3343. https://doi.org/10.1016/j.ceramint.2021.10.108.
[17] P. Himakar, N Murali, D Parajuli, V Veeraiah, K Samatha, TW Mammo, Magnetic and DC electrical properties of Cu doped Co-Zn nano ferrites, J. Electron. Mater. 50, 3249-3257. https://doi.org/10.1007/s11664-021-08895-8.
[18] M. Hadi, KM Batoo, A Chauhan, OM Aldossary, R Verma, Y Yang, Tuning of structural, dielectric, and electronic properties of Cu doped Co-Zn ferrite nanoparticles for multilayer inductor chip applications, Magnetochemistry 7 (4), 53. https://doi.org/10.3390/magnetochemistry7040053.

[19] A. Sukata, G. Mezinskis, Sol-gel auto-combustion synthesis of spinel-type ferrite nano-materials, J. Fron. Mater. Sci. 6 (2012) 128, https://doi.org/10.1007/s11706-012-0167-3.

[20] X. Huang, J. Zhang, W. Wang, T. Sang, B. Sang, H. Zhu, W. Rao, C. Wong, Effect of pH value on electromagnetic loss properties of Co-Zn ferrite via co-precipitation method, J. Magn. Magn Mater. 405 (2015) 36, https://doi.org/10.1016/j.jmmm.2015.12.051.

[21] K. Sun, Z. Lan, Z. Yu, L. Li, J. Huang, X. Zhao, Grain growth, densification and magnetic properties of NiZn ferrites with Bi_2O_3 additive, J. Phys. D Appl. Phys. 41 (2008) 235002. https://iopscience.iop.org/article/10.1088/0022-3727/41/23/23500.

[22] J.B. Nelson, D.P. Riley, An experimental investigation of extrapolation methods in the derivation of accurate unit-cell dimensions of crystals, Proc. Phys. Soc., London 57 (1945) 160. https://iopscience.iop.org/article/10.1088/0959-5309/57/3/302.

[23] A.A. Satter, H. El-Sayed, M. El-Shokrofy, M.K, M.M. El-Tabey, Improvement of the magnetic properties of Mn-Ni-Zn ferrite by the non-magnetic Al^{3+} ion substitution, J. Appl. Sci. 5 (2005) 162, https://doi.org/10.3923/jas.2005.162.168.

[24] B.D. Cullity, Elements of X-Ray Diffraction Reading, third ed., Wesley, Massachusetts, 1972.

[25] Tyunina, M., Peräntie, J., Kocourek, T., Saukko, S., Jantunen, H., Jelinek, M., & Dejneka, A., Oxygen vacancy dipoles in strained epitaxial BaTiO3 films. Phys. Rev. Res., 2(2). https://doi.org/10.1103/physrevresearch.2.023056.

[26] R. D. Lide, in: In CRC Handbook of Chemistry and Physics, 76th ed., CRC Press, I. Dhimanondon, 1995.

[27] De Laeter, John R.; Böhlke, John Karl; De Bièvre, P.; Hidaka, H.; Peiser, H. S.; Rosman, K. J. R.; Taylor, P. D. P, Atomic weights of the elements. Review 2000 (IUPAC Technical Report) Pure and Applied Chemistry. https://doi.org/10.1351/pac200375060683.

[28] S.V. Trukhanov, L.S. Lobanovski, M.V. Bushinsky, V.A. Khomchenko, V.V. Fedotova, I.O. Troyanchuk, H. Szymczak, Microstructure evolution and magnetoresistance of the A-site ordered Ba-doped manganites, Semiconductors 41 (5) (2007) 507–511, https://doi.org/10.1134/S1063782607050041.

[29] V.D. Doroshev, V.A. Borodin, V.I. Kamenev, A.S. Mazur, T.N. Tarasenko, A.I. Tovstolytkin, S.V. Trukhanov, Self-doped lanthanum manganites as a phase-separated system: transformation of magnetic, resonance, and transport properties with doping and hydrostatic compression, J. Appl. Phys. 104 (2008), https://doi.org/10.1063/1.3007993, 093909-9.

[30] M. Yan, F.D. Johnson, Impurity-induced exaggerated grain growth in Mn-Zn ferrite, J. Am. Ceram. Soc. 61 (1978) 342, https://doi.org/10.1111/j.1151-2916.1978.tb09325.x.

[31] H. Shokrollahi, Magnetic properties and densification of Manganese–Zinc soft ferrites ($Mn_{1-x}Zn_xFe_2O_4$) doped with low melting point oxides, J. Magn. Magn Mater. 320 (2008) 463–474, https://doi.org/10.1016/j.jmmm.2007.07.003.

[32] E.V. Gopalan, K.M. Malini, S. Saravanan, D.S. Kumar, Y. Yoshida, M.R. Anantharaman, Evidence for polaron conduction in nanostructured Manganese ferrite, J. Phys. D. 41 (2008) 1850. https://iopscience.iop.org/article/10.1088/0022-3727/41/18/185005.

[33] C. Zhang, P.D. Bristowe, First-principles calculations of oxygen vacancy formation in barium-strontium-cobalt-ferrite, RSC Adv. 3 (2013) 1226712274, https://doi.org/10.1039/C3RA41585F.

[34] I. O. Troyanchuk, S. V. Trukhanov, D. D. Khalyavin, H. Szymczak, Magnetic properties of anion deficit manganites Ln0.55Ba0.45MnO3-γ (Ln=La, Nd, Sm, Gd, γ≤0.37), J. Magn. Magn Mater. 208 (2000) 217-220. https://doi.org/10.1016/S0304-8853(99)00529-6.

[35] S.V. Trukhanov, D.P. Kozlenko, A.V. Trukhanov, High hydrostatic pressure effect on the magnetic state of anion-deficient $La_{0.70}Sr_{0.30}MnO_x$ perovskite manganites, J. Magn. Magn Mater. 320 (2008) e88–e91, https://doi.org/10.1016/j.jmmm.2008.02.021.

[36] S.V. Trukhanov, I.O. Troyanchuk, N.V. Pushkarev, H. Szymczak, Magnetic properties of anion-deficient $La_{1-x}Ba_xMnO_{3-x/2}$ ($0 \le x \le 0.30$) manganites, J. Exp. Theor. Phys. 96 (2003) 110–117, https://doi.org/10.1134/1.1545390.

[37] S.V. Trukhanov, M.V. Bushinsky, I.O. Troyanchuk, H. Szymczak, Magnetic ordering in $La_{1-x}Sr_xMnO_{3-x/2}$ anion-deficient manganites, J. Exp. Theor. Phys. 99 (2004) 756–765, https://doi.org/10.1134/1.1826167.

[38] V.T. Zaspalis, V. Tsakaloudi, M. Kolenbrander, The effect of dopant on the incremental permeability of MnZn ferrites, J. Magn. Magn Mater. 313 (2007) 29–36, https://doi.org/10.1016/j.jmmm.2006.11.210.

[39] E. Shirsath Sagar, B.G. Toksha, R.H. Kadam, S.M. Patange, D.R. Mane, Doping effect of Mn^{2+} on the magnetic behavior in Ni-Zn ferrite nanoparticles prepared by sol-gel auto combustion, J. Phys. Chem. Solid. 71 (2010) 1669, https://doi.org/10.1016/j.jpcs.2010.08.016.

[40] S.S. Jadhav, E. Shirsath, B.G. Toksha, S.J. Shukla, K.M. Jadhav, Chin. J. Chem. Phys. 21 (2008) 381, https://doi.org/10.4028/www.scientific.net/JNanoR.34.9.

[41] J. Hu, M. Yan, Preparation of high permeability Ni-Cu-Zn ferrites, J. Zhej. Univ. Sci. 6B (2005) 580, https://doi.org/10.1631/jzus.2005.b0580.

[42] T. Tsutaoka, T. Ueshima, T. Tokunaga, T. Nakamura, K. Hatakeyama, Frequency dispersion and temperature variation of complex permeability of Ni-Zn ferrite composite materials, J. Appl. Phys. 78 (1995) 3983, https://doi.org/10.1063/1.359919.

[43] K. J. Overshoot, The Causes of the Anomalous Loss in Amorphous Ribbon Materials, IEEE Trans. Magn., 17(6), 2698–2700. https://doi.org/10.1109/tmag.1981.1061648.

[44] R. Valenzuela, Magnetic Ceramics, Cambridge University Press, Cambridge, 1994.

[45] A.A. Sattar, A.H. Wafik, K.M. El-Shokrofy, M.M. El-Tabby, Magnetic properties of Cu–Zn ferrites doped with rare earth oxides, J. Phys. Status Solidi 117 (1999) 563, https://doi.org/10.1002/(sic)1521-396x, 199902)171:2<563::aid-pssa563>3.0.co;2-k.

[46] S.H. Kang, H. I Yoo, The effect of nonstoichiometric (δ) on the magnetic properties of $(Mg_{0.22}Mn_{0.07}Fe_{0.71})_{3-\delta}O4$ ferrite, J. Appl. Phys. 88 (2000) 4754–4757, https://doi.org/10.1063/1.1312844.

[47] Jain, G. C., Das, B. K., Khanduja, R. S., & Gupta, S. C., Effect of intragranular porosity of initial permeability and coercive force in a manganese zinc ferrite, J. Mater. Sci., 11 (7), 1335–1338. https://doi.org/10.1007/bf00545155.

[48] A.P. Globus, P. Duplex, Effective anisotropy in polycrystalline materials separation of components, J. Appl. Phys. 39 (1968) 727, https://doi.org/10.1063/1.216360.

[49] S. Chikazumi, S. Charap, in: In Physics of Magnetism, John Wiley & Sons, New York, 1964, p. 140.

[50] P.B. Pandya, H.H. Joshi, R.G. Kulkarni, Bulk magnetic properties of Co-Zn ferrites prepared by co-precipitation method, J. Mater. Sci. 26 (1991) 5509, https://doi.org/10.1007/BF00553651.

[51] S.T. Mahmud, A. K. M. Akther Hossain, A.K.M. Abdul Hakim, M. Seki, T. Kawai, H. Tabata, Influence of microstructure on the complex permeability of spinel type N-Zn ferrite, J. Magn. Magn Mater. 305 (2006) 269, https://doi.org/10.1016/j.jmmm.2006.01.012.

[52] Badreldin Ahmed, E. Aya, Abusrafa & Ahmed Abdel-Wahab, Oxygen-deficient perovskites for oxygen evolution reaction in alkaline media: a review, J. Emergent Mater. 3 (2020) 567–590, https://doi.org/10.1007/s42247-020-0.

[53] S. Krupicka, One-ion model for the magnetic anisotropy in the system $Mn_xFe_{3-x}O_4$, J. Phys. Status Solidi 4 (1964) 117, https://doi.org/10.1515/9783112495582-026.

[54] Singh, Amarendra K.; Goel, T. C.; Mendiratta, R. G.; Thakur, O. P.; Prakash, Chandra, Magnetic properties of Mn substituted Ni–Zn ferrites, J. Appl. Phys., 92 (7), 3872. https://doi.org/10.1063/1.1504493.

[55] Jinlong Li, Yu Zhong, Ke Sun, Xiaona Jiang, Zhiyong Xu, Zhongwen Lan, Grain growth kinetics and magnetic properties of NiZn ferrite thin films, J. Alloys Compd. 513 (2012) 606–609, https://doi.org/10.1016/j.jallcom.2011.11.022.

[56] Singh, Amarendra K.; Goel, T. C.; Mendiratta, R. G.; Thakur, O. P.; Prakash, Chandra, Dielectric properties of Mn-substituted Ni–Zn ferrites, J. Appl. Phys., 91 (10), 1. https://doi.org/10.1063/1.1470256.

[57] P.K. Roy, J. Bera, Characterization of Nano-crystalline Ni-Cu-Zn ferrite powders synthesized by sol-gel auto-combustion method, J. Mater. Process. Technol. 197 (2008) 279–283, https://doi.org/10.1016/j.jmatprotec.2007.06.027.

[58] M.H.R. Khan, A. K. M. Akther Hossain, Reentrant spin glass behavior and large initial permeability of $Co_{0.5-x}Mn_xZn_{0.5}Fe_2O_4$, J. Magn. Magn Mater. 324 (2012) 550–558, https://doi.org/10.1016/j.jmmm.2011.08.039.